CRITICAL LEVELS AND WAVEBREAKING IN 3D OROGRAPHIC FLOWS

Vanda Grubišić
National Center for Atmospheric Research
Boulder, Colorado, U.S.A.

1. INTRODUCTION

The importance of critical levels in geophysical flows stems from their omnipresence and complex wave/mean-flow interactions in their vicinity. A critical level is a surface at which the Doppler-shifted frequency $\omega' = \vec{U} \cdot \vec{\kappa} - \omega$ of a plane wave with the horizontal wavenumber vector $\vec{\kappa}$ and frequency ω vanishes. For mountain waves resulting from a steady forcing by the flow over topography, $\omega = 0$ and the critical levels arise wherever $\vec{U} \cdot \vec{\kappa} = 0$. The name *critical* derives from the singularity of the linearized inviscid time-independent equations (and their solutions) at such levels (Miles 1961; Booker and Bretherton 1967), indicating that the transience, momentum and heat diffusion as well as nonlinear steepening and amplification of waves are important in their vicinity (Maslowe 1986; chap 4.11 in Baines 1995). For the local Richardson number $\mathrm{Ri}\,(\equiv N^2/U_z^2) \gg 1/4$ at a critical level, linear inviscid theory predicts that infinitesimal perturbations are smoothly absorbed and deposit their momentum into the mean flow below the critical level. Whether this occurs in reality, depends on the amplitude of perturbations as well as the effectiveness of viscous processes in preventing nonlinear steepening and wavebreaking.

In atmospheric flows over complex terrain, gravity waves encounter their critical levels, in general, at different altitudes where the projection of the mean velocity $\vec{U}(z)$ on a given wavenumber vector $\vec{\kappa} = (k, l)$ vanishes. A number and location of critical levels is determined by a degree of directional wind shear and topographic spectrum. The associated filtering of orographic gravity waves in directional wind shear is discussed by Shutts elsewhere in this volume. In this paper, which is largely based on work by Grubišić and Smolarkiewicz (1997), we address primarily unidirectional, steady, constant-shear flows with a critical level located where $U = 0$. In section 2 we review the analytical model and describe its steady-state solutions consisting of a 3D wave pattern forced by a small-amplitude isolated axisymmetric

obstacle in the presence of a single critical level. Since linear inviscid solutions are singular at the critical level, we use a numerical model to assess the impact of dissipation and local nonlinearities on the solutions. In section 3 we discuss numerical solutions for both the unidirectional wind profile and a simple case of wind turning with height. We determine, in the parameter space spanned by the nondimensional mountain height $\hat{h}$ ($\equiv h_0 N/U_0$) and the Richardson number Ri, the bounds of a regime in which our linear solutions for the unidirectional wind profile are valid everywhere except in the vicinity of the critical level where numerical solutions, as well as natural flows, are regularized by viscous dissipation (Kelly 1977; Worthington and Thomas 1996). Beyond this regime, wavebreaking can be expected to occur in 3D flows with a single critical level. In section 3.3 we comment briefly on the effect of wind turning with height on the existence and location of wavebreaking. Conclusions are presented in section 4.

2. ANALYTIC SOLUTIONS

The linear analytic model of a stably-stratified, inviscid, non-rotating, hydrostatic flow past a small-amplitude, gently-sloped 3D hill is based on the incompressible Boussinesq approximation of the Euler equations cast in the Cartesian framework (x, y, z) and linearized with respect to a hydrostatically balanced reference-state. The model equations are

$$\rho_0 U u_x + \rho_0 w U_z = -p_x \ , \tag{1a}$$

$$\rho_0 U v_x = -p_y \ , \tag{1b}$$

$$0 = -p_z - \rho g \ , \tag{1c}$$

$$u_x + v_y + w_z = 0 \ , \tag{1d}$$

$$U\rho_x + w\bar{\rho}_z = 0 \ , \tag{1e}$$

where (u, v, w) are the perturbation velocity components, and $p = p(x, y, z)$ and $\rho = \rho(x, y, z)$ are the perturbation pressure and density, respectively. The reference state density is $\bar{\rho}(z) = \rho_0(1 - N^2 z/g)$, where the Brunt-Väisälä frequency N and the reference density ρ_0 are assumed constant. The ambient velocity profile

$$U(z) = U_0 \left(1 - \frac{z}{z_c}\right) \ , \tag{2}$$

has a critical level at $z = z_c$. The hydrostatic approximation is justified given $k \ll N/U(z = 0) < \infty$, since when the wind decreases with height, the importance of non-hydrostatic effects

decreases aloft. Our analysis is limited to Ri $> 1/4$, sufficient for the stability of a parallel, stratified, inviscid, incompressible flow with respect to the Kelvin-Helmholtz waves (Drazin and Reid 1971).

Equations (1a)–(1e) can be solved for w, or equivalently, for the vertical displacement of isopycnal surfaces $\eta \equiv z(x,y;z_0) - z_0$, where z_0 is the upstream height of a given isopycnal surface. The w and η fields are related through the linearized kinematic condition $w \equiv \dot{\eta} \approx U\eta_x$, whereas ρ can be expressed in terms of η as $\rho = -\bar{\rho}_z\eta$ in lieu of (1e). Using the Fourier integral representation of solutions and introducing a new variable $\zeta = z - z_c$ leads to a following form of the equation for the vertical structure of the Fourer modes $\tilde{\eta}(k,l,z)$

$$\zeta^2\,\tilde{\eta}_{\zeta\zeta} + 2\,\zeta\,\tilde{\eta}_{\zeta} + \mathrm{Ri}\,\frac{\kappa^2}{k^2}\,\tilde{\eta} = 0 \ , \tag{3}$$

where $\mathrm{Ri} \equiv (N/U_z)^2 = (Nz_c/U_0)^2$, $\kappa^2 \equiv k^2 + l^2$, and k and l are horizontal wavenumbers in the x and y directions. Equation (3) is subject to

$$\tilde{\eta}(k,l,z=0) \ = \ \tilde{h}(k,l) \ , \tag{4}$$

and the radiation boundary condition aloft. In (4), $\tilde{h}(k,l)$ denotes the Fourier transform of the mountain shape. The equation (3) is solved for a class of constant-shear flows past a bell-shaped mountain $h(r) = h_0(\,1 + r^2/a^2\,)^{-3/2}$, $r \equiv (x^2+y^2)^{1/2}$. Further details of the mathematical model and solution techniques can be found in Grubišić and Smolarkiewicz (1997). In the following we briefly describe properties of the linear analytic solutions. The displacement fields below and above the critical level are shown in Fig. 1. Below the critical level, the wave pattern bears resemblance to that characteristic of the constant mean flow (Smith 1980). Above the critical level, however, it is significantly different as the wave components emerge strongly attenuated by the factor

$$\exp\left\{-\pi\left[\mathrm{Ri}\,(\cos\varphi)^{-2} - 1/4\right]^{1/2}\right\} \ . \tag{5}$$

Here φ represents the angle between the horizontal wavenumber vector $\vec{\kappa}$ and the direction of the mean flow. In this directional filtering, the components with wave fronts parallel to the mean flow ($\varphi = \pi/2$) are almost entirely removed leaving only components with wave fronts perpendicular or nearly perpendicular to the mean flow.

Infinitesimally close beneath the critical level, wave solutions oscillate rapidly and the local vertical wavenumber and displacements become infinite. Similar as in 2D, in the limit $z \nearrow z_c$, the vertical velocity, which is proportional to $(z_c - z)^{1/2}$, becomes infinitesimally small

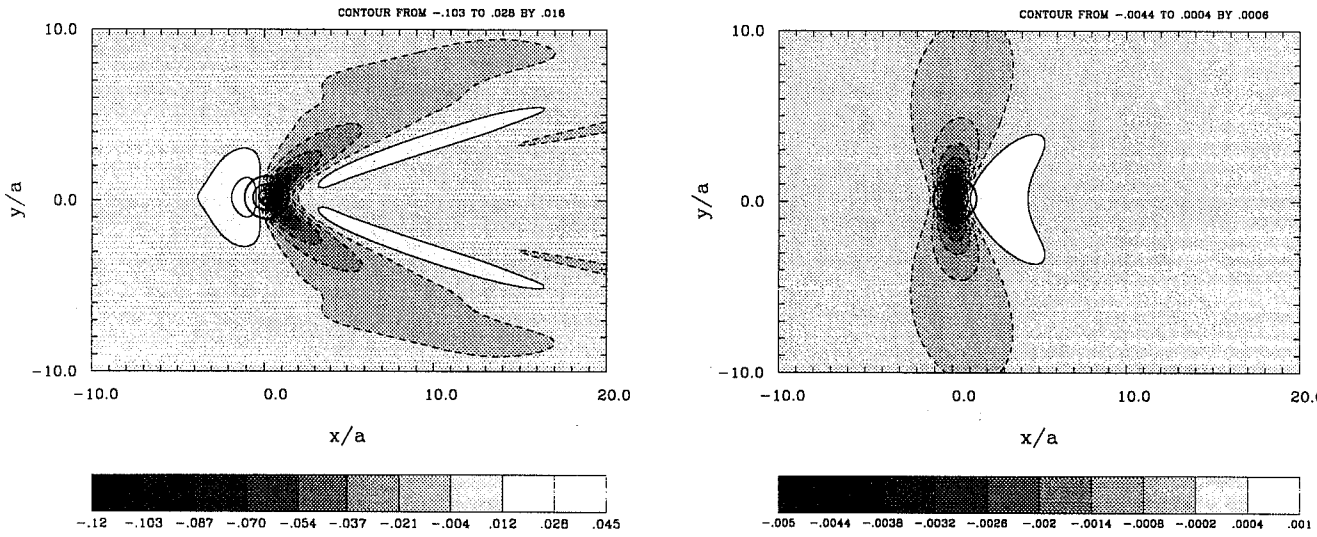

Figure 1: FFT representations of the displacement fields of the isopycnals with the undisturbed heights $z_c(1 \pm 0.15)$ below (left panel) and above (right panel) the critical level, respectively. The mean flow (with Ri = 1 and $\hat{h} = 0.1$) is from left to right. The mountain is displayed using thick solid lines with the contour interval 0.025 $\hat{h}$.

whereas both horizontal velocity components, proportional to $(z_c - z)^{-1/2}$, tend to infinity. This indicates that, at least in the linear approximation, motions become progressively more horizontal as the critical level is approached. It also indicates that the shear in the vicinity of critical level will be large, leading eventually to the breakup of waves through the shearing or convective instability. Below the critical level, the paraboloidal wave envelopes (locus of points where the wave amplitude is maximal) have the following form

$$\hat{y}^2 = \frac{\sqrt{c}}{2} \frac{\hat{r}}{\hat{r}_c} \hat{x} \left| \ln\left(1 - \frac{2\hat{z}}{\sqrt{c}}\right)\right|, \tag{6}$$

where $\hat{r} \equiv [\,\hat{x}^2 + \hat{y}^2\,]^{1/2}$, $\hat{r}_c \equiv [\,\hat{x}^2 + (1 - c^{-1}\hat{y}^2)\,]^{1/2}$, $\hat{x} \equiv x/a$, $\hat{y} \equiv y/a$, $\hat{z} \equiv z\ N/U_0$, and $c = 4\mathrm{Ri} > 1$. On approaching the critical level, the envelopes widen with height (Fig. 2) so that infinitesimally below the critical level they become plane surfaces perpendicular to the mean flow direction.

The pressure perturbation at the ground is characterized by a fore-and-aft asymmetry with a stronger positive pressure anomaly over an upwind slope, and a weaker negative anomaly farther in the lee. As a consequence of this shear-reduced positive correlation between the pressure anomalies and the mountain slopes, drag is always smaller than in the uniform wind case. For both positive and negative linear mean shear, mountain wave drag is equal to

$$D = \frac{1}{3}\rho_0 N U_0 a h_0^2 \left[(c-1)\mathbf{K}\left(c^{-1/2}\right) + (2-c)\mathbf{E}\left(c^{-1/2}\right)\right] , \tag{7}$$

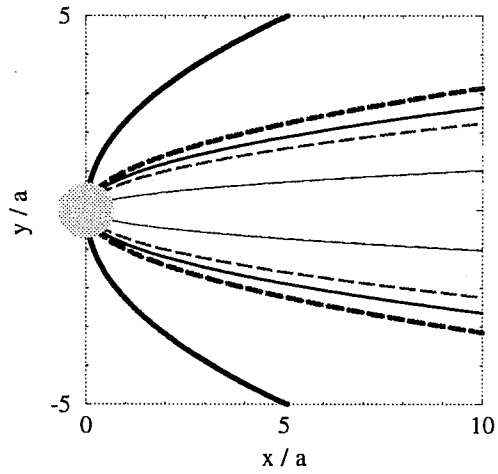

Figure 2: Asymptotic wave envelopes for mean flows with a linear negative shear (Ri = 1, $\hat{h} = 0.1$, solid lines) and zero shear (Ri = ∞, $\hat{h} = 0.1$, dashed lines) at elevations $\hat{z} = 0.1$ (thin lines), $\hat{z} = 0.5$ (medium lines), and $\hat{z} = 0.99$ (thick lines). The shaded circle at the origin illustrates the approximate size of the obstacle at half of its height.

where **K** and **E** denote the elliptic integrals of the first and second kind, respectively, and $c = 4\mathrm{Ri} > 1$. Figure 3 displays D as a function of Ri normalized by $\lim_{\mathrm{Ri}\to\infty} D = \pi/4\ \rho_0 N U_0 a h_0^2$. As $\mathrm{Ri} \to 1/4$, $\lim_{\mathrm{Ri}\to 1/4} D = 1/3\ \rho_0 N U_0 a h_0^2$, and, in contrast to equivalent 2D flows (Smith 1986), drag does not vanish. Zero drag in 2D flows is a consequence of a fore-and-aft symmetry of the linear solutions at strong shears. In 3D, this symmetry is maintained only for modes with wave fronts normal to the mean flow, whereas all others induce asymmetric pressure perturbations leading to a non-zero drag.

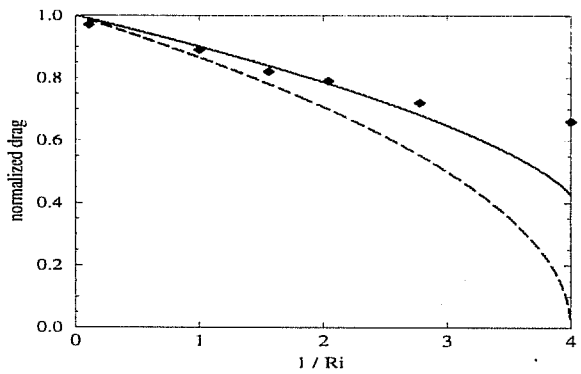

Figure 3: Mountain-wave drag (normalized by $D_0 = \pi/4\ \rho_0 N U_0 a h_0^2$) as a function of the inverse mean-flow Richardson number. The solid curve represents the analytic result (7), and the dashed curve the corresponding 2D result $D_{2D}/D_0 = [1 - 1/(4\mathrm{Ri})]^{1/2}$ (with $a = 1$ in D_0). Diamonds display numerical results discussed in section 3.1.

In the remainder of this paper we compare numerical and analytical solutions, in order to assess the realizability of the linear solutions as well as the impact of local nonlinearities and dissipation on the singularities predicted by the linear model for unidirectional flows. We also discuss a transition to the nonlinear regime characterized by wavebreaking aloft both in unidirectional and flows in which the environmental wind turns with height.

3. NUMERICAL SOLUTIONS

The numerical model used in this study has been described in Smolarkiewicz and Margolin (1997). It is representative of a class of nonhydrostatic atmospheric models that solve the anelastic equations of motion in the standard nonorthogonal terrain-following coordinates. Here, we present selected results from a series of over 30 experiments with $\hat{h} \leq 0.3$ and $\mathrm{Ri} \in [0.25, 9]$. In all experiments $U_0 = 10$ ms^{-1}, $N = 0.01$ s^{-1}, $a = 5000$ m, resulting in $U_0/Na = 0.2$ and the mostly hydrostatic perturbations. The physical domain, $20a \times 20a \times 3z_c$, with the mountain centered in $z = 0$ plane, is covered with $81 \times 81 \times 91$ grid points. Further details on the numerical model and experimental setups can be found in Grubišić and Smolarkiewicz (1997).

3.1 Unidirectional flows: Linear Regime

Figure 4 shows a regime diagram of the $(\hat{h}, \mathrm{Ri})$ parameter space. The shaded region represents the "linear regime" where numerical solutions achieve steady state and agree closely with the linear predictions. In Fig. 5, the linear-regime solution (run LS1) for weak shear ($\mathrm{Ri} = 9$) is illustrated with u-velocity perturbation in the central xz-plane. In accordance

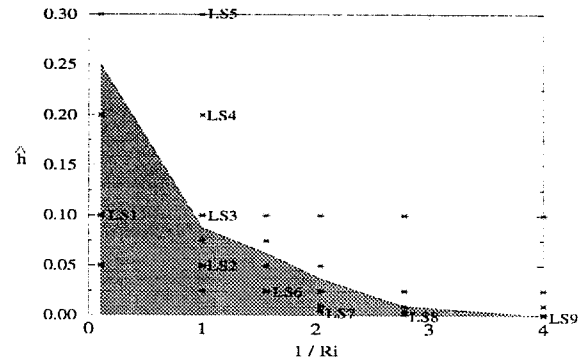

Figure 4: Regime diagram of the critical-level flow past an axisymmetric obstacle for linearly-sheared ambient wind. Stars and text labels denote performed numerical experiments, and the shaded region represents the "linear regime".

with the analytical predictions, as the waves approach the critical level, the vertical wavelength diminishes and the wave motions become increasingly more horizontal. Within the linear regime, a good agreement between the analytical and numerical solutions is found everywhere, except in the vicinity of the critical level where numerical solutions are regularized by implicit viscosity of finite-difference approximations (Smolarkiewicz and Pudykiewicz 1992; Prusa et al. 1996), which mimics the dissipation inevitable in turbulent critical-level flows. As a result, the waves approaching the critical level are smoothly absorbed as they

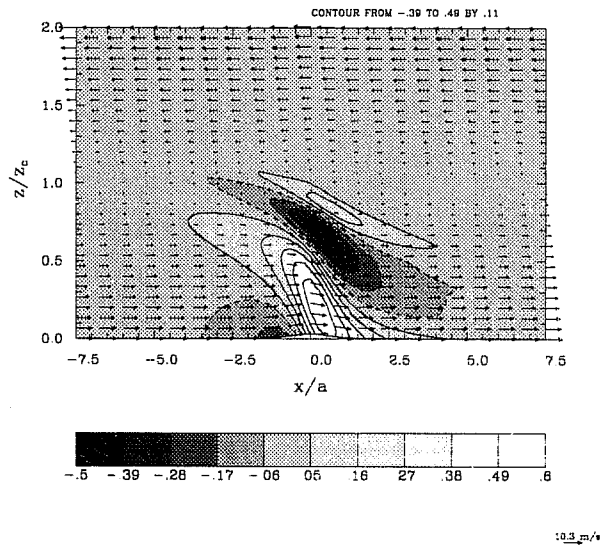

Figure 5: Perturbation of the u-velocity component in the central xz-plane from experiment LS1. Vectors represent the total velocity.

deposit their momentum into the mean flow. This is reflected in the profile of the vertical flux of horizontal momentum $< u\,w > \equiv \int_{-\infty}^{+\infty}\int_{-\infty}^{+\infty} u\,w\,dx\,dy$, (Fig. 6), which displays strong divergence for $0.75z_c < z < z_c$, above a deep layer of constant momentum flux (cf. Eliassen and Palm 1960; Broad 1995). Above the critical level, the flux is strongly attenuated and the small positive values indicate the presence of upward-propagating waves in the reversed mean flow—a residual transmission through the critical level.

3.2 Unidirectional flows: Transition to a Nonlinear Regime

From the regime diagram in Fig. 4 it is evident that linear analytic solutions, predicting smooth wave absorption at the critical level, are valid for a range of mountain heights at Ri > 1. The larger the Richardson number, the higher the threshold mountain height at which the pile up of energy beneath the critical level will eventually lead to a nonlinear wave amplification there. However, for a linear velocity profile, large Richardson numbers imply

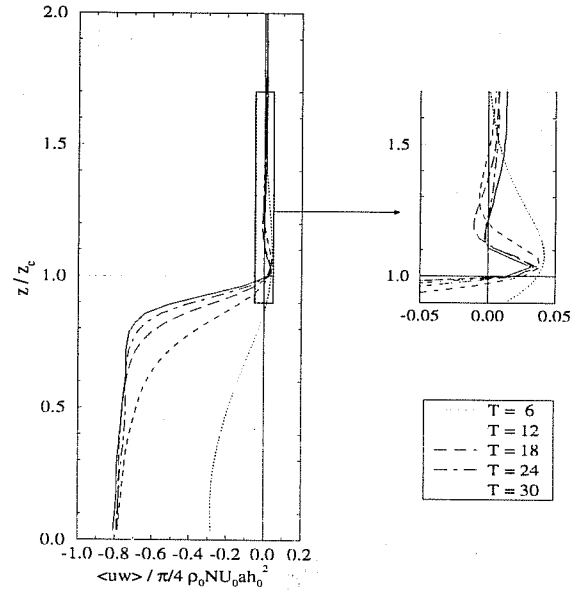

Figure 6: Profiles of the normalized vertical flux of the horizontal momentum $< u\,w >$ from experiment LS7. $T = tU_0/a$ denotes nondimensional time.

weak vertical wind shear and critical levels at altitudes above those at which waves would steepen and break in a case of constant (or weakly-sheared) wind profile. Thus, in order to illustrate the transition from the linear regime, discussed in the previous section, to the nonlinear regime characterized by wavebreaking above the mountain and beneath the critical level, we chose experiments with Ri = 1 (LS3–LS5). For experiment LS3 (located near the regimes' interface in Fig. 4) nonlinear effects are weak and linear theory still provides a qualitatively meaningful description of the flow. Farther into the nonlinear regime (runs LS4, LS5), large amplitude perturbations are not confined anymore to the vicinity of the

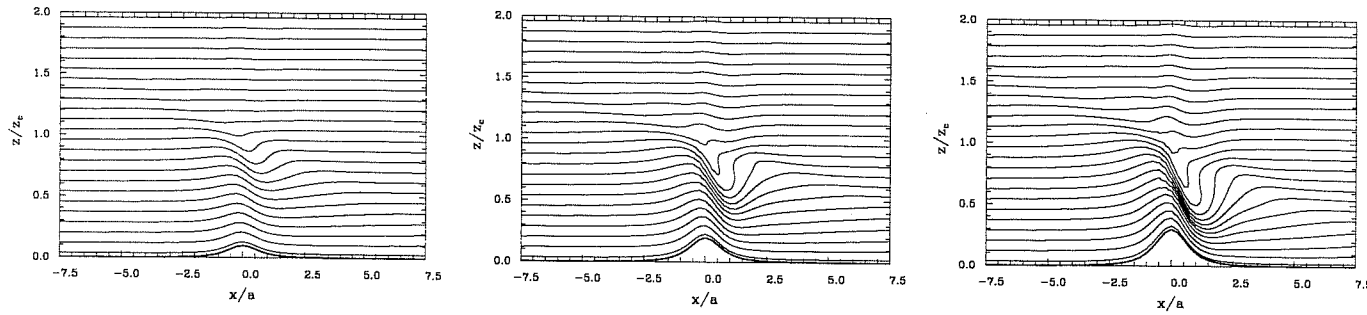

Figure 7: Numerical solutions from experiments LS3–LS5 (the nonlinear regime). From left to right: i) isentropes in the central xz-plane from the experiment LS3 (Ri = 1.0, $\hat{h} = 0.1$); ii) as in i) but for experiment LS4 (Ri = 1.0, $\hat{h} = 0.2$); iii) as in plate i) but for experiment LS5 (Ri = 1.0, $\hat{h} = 0.3$).

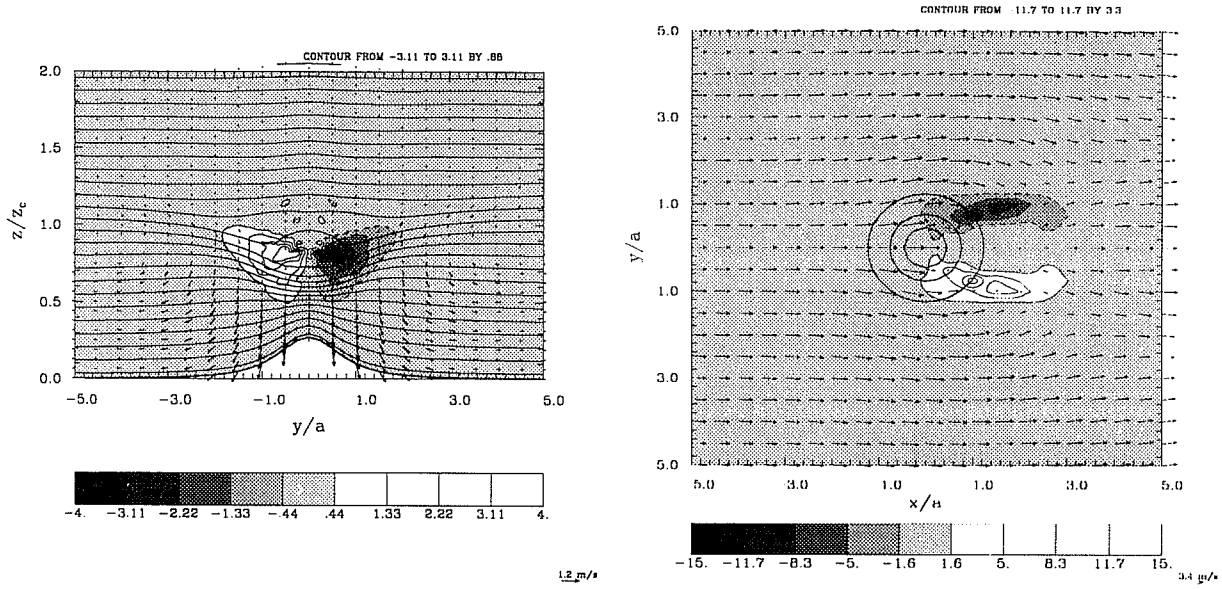

Figure 8: Normalized potential vorticity ($\times 10^{-4}$ s^{-1}) from numerical experiment LS5 (Ri = 1.0, $\hat{h} = 0.3$) in the yz-plane at $x = a/4$ (left); b) in the horizontal plane at $z = 0.8z_c$ (right).

critical level but affect the flow everywhere above the lee slopes (Fig. 7). Numerical solutions in Fig. 7 are snapshots at a point at which these flows were still evolving in time. Later into the simulations, flows in this regime are similar to those discussed by Miranda and Valente (1997) and by Miranda elsewhere in this volume, except that wakes in our solutions remain steady. The dissipative nature of the wave/mean-flow interaction in the wavebreaking region beneath the critical level gives rise to the "effective force" that the dissipating waves exert on the mean flow causing it to decelerate (McIntyre and Norton 1990). Within this dissipative zone the inviscidly generated vorticity (due to the tilting in vertical of the mean vorticity vector plus baroclinically generated vorticity by the wave field) is diffused onto isentropic surfaces giving rise to the PV anomalies downstream (Rotunno et al. 1998). Figure 8 illustrates these PV anomalies displaying normalized potential vorticity $PV' \equiv \vec{\Omega} \cdot \nabla\theta / |\nabla\theta|$, where $\vec{\Omega}$ denotes the total vorticity vector (including the ambient component $U_z\hat{y}$). These PV banners aloft (with amplitude $\sim$ 10% $|\vec{\Omega}|$) originate from the wavebreaking region and surround the stagnant region in the lee of the mountain.

3.3 Wind turning with height

A simple extension of the unidirectional wind profile (2) to a case of wind turning with height is provided by adding a constant component of the wind in the y-direction

$$(U(z), V(z)) = \left[U_0\left(1 - \frac{z}{z_c}\right), V_0\right] = [\alpha\zeta, V_0] \quad , \tag{8}$$

where $\zeta \equiv z - z_c$, and $\alpha \equiv -U_0/z_c$. The resulting wind rotates counterclockwise with height as indicated in Fig. 9. According to Shutts (1995), from a full spectrum of waves launched by a flow over an axisymmetric hill and propagating upward in such an environment, a range of waves with wavenumber vectors perpendicular to the encountered wind directions will be selectively filtered out by critical level absorption. For profile (8) this implies absorption of a range of wave numbers from the first and fourth quadrants. For these waves, the critical levels are located at

$$\mathcal{Z}(k,l) = z_c - \frac{V_0 \tan\theta_c}{\alpha} \quad , \tag{9}$$

where z_c is the altitude at which $U = 0$, and $\tan\theta_c = l/k$. With the critical levels being spread out in vertical, it is reasonable to expect the flow to be less singular, and wavebreaking less likely to occur. In Fig. 10 we illustrate this with the results of two experiments for $\hat{h} = 0.2$ and 0.3, Ri = 1, and V_0=5 ms^{-1}. The respective solutions for the unidirectional wind profile ($V_0 = 0$) are shown in Figs. 7b,c. For the wind profile turning with height, the strongest flow perturbations are still found in the proximity of z_c, the altitude at which a large portion of the spectrum ($k \neq 0$, $l = 0$) finds its critical level. However, the perturbations extend beyond this level as the waves that have not yet encountered their critical levels continue to propagate upward. The large amplitude perturbations lie downstream of the mountain in the central yz-plane as the wind vectors near z_c are oriented mostly in the positive y-direction. The degree of nonlinearity in these solutions is still significant and might lead to

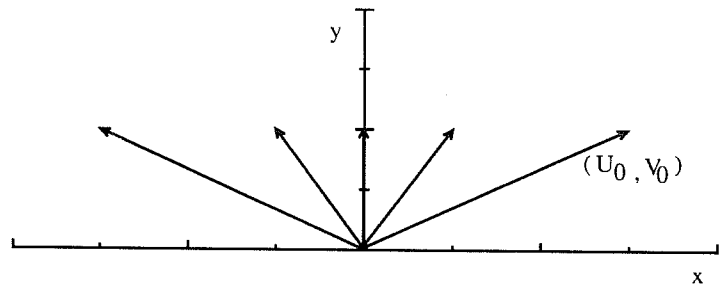

Figure 9: Wind vectors turning counterclockwise with height from the surface direction labeled as (U_0, V_0).

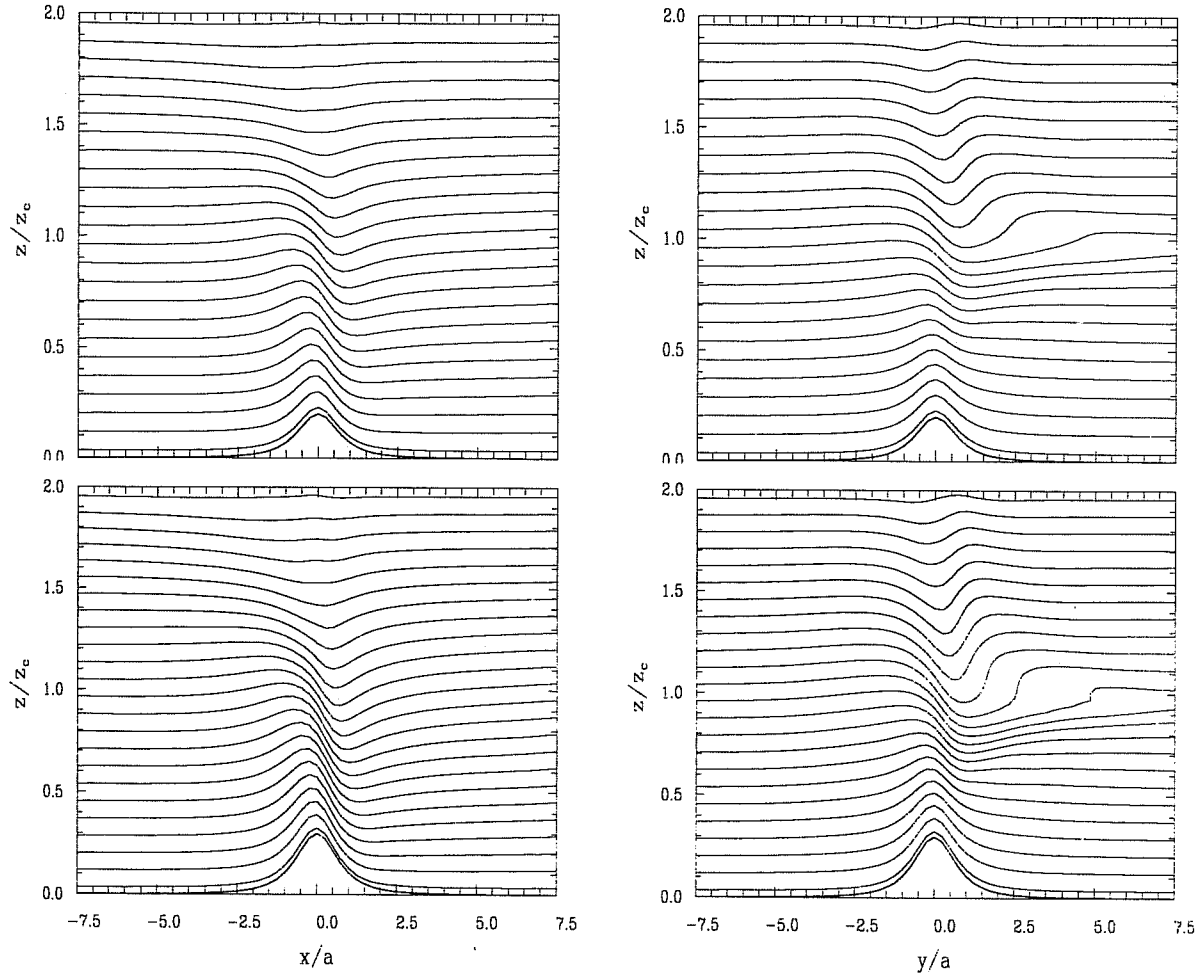

Figure 10: Numerical solutions at $T = tU_0/a = 18$ for the wind profile turning with height. Isentropes in the central xz-plane (left) and yz-plane (right) for Ri $= 1.0$, $\hat{h} = 0.2$ (top) and Ri $= 1.0$, $\hat{h} = 0.3$ (bottom).

wavebreaking at later times and farther away from the mountain. However, it is apparent that in the case of wind turning with height larger mountain heights are necessary to induce wavebreaking aloft than for the unidirectional profile. For any particular wind profile, such as (8), the degree of singularity is likely to depend on the orographic spectrum as well.

4. CONCLUSIONS

Using linear theory and numerical simulations, we have examined a three-dimensional, linear field of stationary internal gravity waves in a vertically sheared, unidirectional flow past an isolated axisymmetric mountain. The assumed linear ambient wind profile and constant environmental stability constitute perhaps the simplest scenario which provides a critical level for all wave components at the height where the mean flow vanishes. Our linear theory, formally valid for Ri $> 1/4$, is hydrostatic, Boussinesq, irrotational, and inviscid. The

stationary wave pattern similar to the one for the constant wind profile has energy concentrated along the paraboloidal wave envelopes which widen on approaching the critical level. Above the critical level perturbations are weak as the waves continuously and systematically transfer their energy to the mean flow beneath the critical level. In an inviscid model, this pile up of energy, compressed vertical wavelength, and the large horizontal excursions that the individual fluid elements undergo beneath the critical level, will eventually lead to overturning of isentropic surfaces.

In view of the intrinsic singularity of the linear theory, we have conducted a series of experiments with a numerical model suitable for simulating natural stratified flows to verify realizability of the analytical results. Our numerical simulations for the unidirectional wind profile confirm the theoretical predictions for a range of mountain heights given $\mathrm{Ri} > 1$. The larger the vertical scale of shear compared to the vertical wavelength of waves, the larger the range of mountain heights for which the linear scenario of smooth wave absorption is likely to occur. Within the linear regime, numerical solutions in the vicinity of the critical level are regularized by the implicit viscosity of finite-difference approximations emulating dissipation in turbulent critical-level flows. The wavebreaking beneath the critical level occurs ultimately at the amplitude of orography at which the nonlinearities begin to dominate over viscous dissipation in the proximity of the critical level. This marks the transition to the nonlinear regime characterized by strongly accelerated flows over the lee slopes and wakes with recirculating eddies. The important question here is whether and where critical-level wavebreaking occurs in a more general case of wind turning with height when individual wave components encounter their critical levels at different altitudes. The indications exist that such flows are less singular in a sense of requiring larger mountain amplitudes to produce wavebreaking aloft. This problem will be pursued farther in future studies.

5. REFERENCES

Baines, P. G., 1995: *Topographic Effects in Stratified Flows.* Cambridge University Press, 482 pp.

Booker, J. R., and F. P. Bretherton, 1967: The critical layer for internal gravity waves in a shear flow. *J. Fluid Mech.*, **27**, 513–539.

Broad, A. S., 1995: Linear theory of momentum fluxes in 3-D flows with turning of the mean wind with height. *Quart. J. Roy. Meteor. Soc.*, **121**, 1891–1902.

Drazin, P. G. and W. H. Reid, 1971: *Hydrodynamic Stability.* Cambridge University Press, 527 pp.

Eliassen, A., and E. Palm, 1960: On the transfer of energy in stationary mountain waves. *Geofys. Publ.*, **22**, 1–23.

Grubišić, V., and P. K. Smolarkiewicz, 1997: The effect of critical levels on 3D orographic flows: Linear regime. *J. Atmos. Sci.*, **51**, 1943–1960.

Kelly, R. E., 1977: Linear and nonlinear critical layer effects on wave propagation. *Geofluidynamical Wave Mathematics, Natl. Sci. Found. Reg. Conf. Math.*, Apllied Mathematics Group, University of Washington, 194–210.

Maslowe, S. A., 1986: Critical layers in shear flows. *Ann. Rev. Fluid Mech.*, **18**, 405–432.

McIntyre, M. E., and W. A. Norton, 1990: Dissipative wave-mean interactions and the transport of vorticity and potential vorticity. *J. Fluid Mech.*, **212**, 403–435.

Miles, J. W., 1961: On the stability of heterogeneous shear flows. *J. Fluid Mech.*, **10**, 496–508.

Miranda, P. M. A., and M. A. Valente, 1997: Critical level resonance in three-dimensional flow past isolated mountain. *J. Atmos. Sci.*, **54**, 1574–1588.

Prusa, J. M., P. K. Smolarkiewicz, and R. R. Garcia, 1996: On the propagation and breaking at high altitudes of gravity waves excited by tropospheric forcing. *J. Atmos. Sci.*, **53**, 2186–2216.

Rotunno, R., V. Grubišić, and P. K. Smolarkiewicz, 1998: Vorticity and potential vorticity in mountain wakes. To be submitted to *J. Atmos. Sci.*.

Shutts, G., 1995: Gravity-wave drag parametrization over complex terrain: The effect of critical-level absorption in directional wind-shear. *Quart. J. Roy. Meteor. Soc.*, **121**, 1005–1021.

Smith, R. B., 1980: Linear theory of stratified hydrostatic flow past an isolated obstacle. *Tellus*, **32**, 348–364.

———, 1986: Further development of a theory of lee cyclogenesis. *J. Atmos. Sci.*, **43**, 1582–1602.

Smolarkiewicz, P. K., and L. G. Margolin, 1997: On forward-in-time differencing for fluids: An Eulerian/semi-Lagrangian nonhydrostatic model for stratified flows. *Atmos. Ocean*, **35**, 127-152.

———, and J. A. Pudykiewicz, 1992: A class of semi-Lagrangian approximations for fluids. *J. Atmos. Sci.*, **49**, 2082–2096.

Worthington, R. M., and L. Thomas, 1996: Radar measurements of critical-layer absorption in mountain waves. *Quart. J. Roy. Meteor. Soc.*, **122**, 1263–1282.